CO$_2$ Sensing Characteristics of a La$_2$O$_3$/SnO$_2$ Stacked Structure with Micromachined Hotplates

Tatsuya Iwata *, Kyosuke Matsuda, Kazuhiro Takahashi and Kazuaki Sawada

Department of Electrical and Electronic Information Engineering, Toyohashi University of Technology, Toyohashi 4418122, Japan; matsuda-k@int.ee.tut.ac.jp (K.M.); takahashi@ee.tut.ac.jp (K.T.); sawada@ee.tut.ac.jp (K.S.)

* Correspondence: iwata@ee.tut.ac.jp

Abstract: Demand for the detection of carbon dioxide (CO$_2$) is increasing in various fields, including air-quality monitoring, healthcare, and agriculture. On the other hand, smart gas sensors, in which micromachined gas sensors are integrated with driving circuits, are desirable toward the development of the society of the internet of things. In this study, micromachined hotplate-based CO$_2$ sensors were fabricated and their characteristics were investigated. The sensors have La$_2$O$_3$/SnO$_2$ stacked layers as a sensing material and Pt interdigitated electrodes. A CO$_2$ response of 2.9 for a CO$_2$ concentration of 1000 ppm was obtained at 350 °C with low power consumption (approximately 17 mW). A relatively large response was obtained compared with previous studies even though a compact sputtered-SnO$_2$ film was used. This high response was speculated to be due to a significant contribution of the resistance component near the electrode. Furthermore, CO$_2$ sensing was successfully performed in the CO$_2$ range of 200–4000 ppm with at least 200-ppm resolution.

Keywords: CO$_2$ sensor; micromachined hotplate; La$_2$O$_3$; SnO$_2$

1. Introduction

Carbon dioxide (CO$_2$) exists in air at a fraction of approximately 400 ppm, and its detection is highly demanded for air-quality monitoring, healthcare, and agriculture. On the contrary, with the development of the internet of things and smart sensors, which have functions of signal processing and communication besides sensing, have attracted much attention. Furthermore, sensor chips, into which these functions are integrated, are favorable for the miniaturization of such smart sensors [1–3].

Till date, non-dispersive infrared absorption (NDIR) type, which shows a wide measurement range and high accuracy (e.g., 0–5000 ppm with ±30 ppm accuracy for K30, Sensair [4]), is most widely used as CO$_2$ sensors. However, it is difficult to integrate a NDIR sensor into a chip due to the necessity of a bulky optical system. On the other hand, electro-mechanical [5], potentiometric [6–8], and conductometric types [9–17] have been proposed as miniature CO$_2$ sensors, feasibly integrated into a chip. In particular, the conductometric-type is most suitable for smart sensors in terms of simplicity of readout circuits and IC-process compatibility. Table 1 compares the properties of various conductometric sensors. La-compound-based sensors show a relatively large response, while their operation temperature is several hundred °C. On the contrary, carbon nanotube [16], graphen oxide [15], and poly(ethyleneimine) (PEI) functionalized-polyaniline (PANI) [17] operate at room temperature (RT), their responses are relatively low. Taking account of the application to smart sensors, in which signal processing is carried out on a chip, a large response is beneficial to obtain a sufficient signal–noise ratio of the output signal. In this regard, La-compound materials are promising for smart CO$_2$ sensors.

Table 1. Comparison of the properties of conductmetric type CO_2 sensors.

Material	Response for 1000-ppm CO_2	Temperature	Ref.
La_2O_3-SnO_2	1.5 [a]	400 °C	[9]
LaOCl-SnO_2 nanowire	4.5	400 °C	[14]
BaTiO-CuO	1.12	300 °C	[13]
Carbon nanotube	1.022 [b]	RT	[16]
Graphene oxide	1.14	RT	[15]
PEI-PANI	1.08	RT	[17]

[a]: for approximately 1100-ppm CO_2; [b]: for 800 ppm CO_2.

As described above, La-compound materials require heating to several hundred °C for sensing CO_2, resulting in large power consumption (typically several hundred mW) and a rise in the temperature of the sensor substrates. Therefore, a micromachined hotplate (MHP), which is a suspended heating structure based on microelectromechanical systems, is employed to thermally isolate the sensors from the surroundings [18]. By employing MHPs, the power consumption for the heating is reduced by more than one order of magnitude. In addition, the temperature rise in the surrounding area of the hotplate is suppressed, and thus, the integration of electronic circuits is also possible [2,19,20]. MHP-based semiconductor gas sensors were reported in the sensing of hydrogen (H_2) [21], carbon monoxide (CO) [2,22,23], and nitrogen oxide (NO_x) [3,24], however, semiconductor CO_2 sensors based on MHPs have not been demonstrated.

On the other hand, the response of semiconductor gas sensors can change with sensor size and the material and structure of electrodes besides the type of materials and their microstructures [25–27]. In addition, although La-based semiconductor sensors show large responses to CO_2 as described above, the responses to CO_2 are still low due to the chemical inertness of CO_2 when compared with those for reactive gases such as CO and H_2. For example, to our best knowledge, LaOCl-functionalized SnO_2 nanowires (SnO_2-NW) [14] showed the highest response of 4.5 for 1000-ppm CO_2 amongst the semiconductor materials for CO_2 detection, as shown in Table 1. Furthermore, its sensor area was 800 μm × 1600 μm, and, thus, a structure with a smaller area and a MHP is required for smart sensors with low power consumption. Taking account of these relatively low responses of CO_2 sensors, the influence of the sensor structure on the response can be a critical issue when the sensor size is to be shrunk. Therefore, CO_2 sensors fabricated on MHPs should be characterized toward the realization of smart CO_2 sensors. In this study, sensor elements with La_2O_3/SnO_2 stacked layers as sensing materials were fabricated on MHPs, and their sensing characteristics were investigated.

2. Experimental Procedure

2.1. Sensor Fabrication

The sensors were fabricated on MHPs. A schematic illustration of the devices is shown in Figure 1, which depicts both top and cross-sectional views, and the white dotted line in the top view indicates the position of the cross section. The MHP has a membrane comprising of stacked layers of silicon dioxide (SiO_2) and silicon nitride (SiN), suspended with four bridges. The heater has a meander-shaped structure, and polycrystalline Si (poly-Si) is used as the heater material. Under the membrane, an approximately 50-μm-thick Si island was formed to maintain a uniform temperature distribution within the membrane. The sensor part comprises the sensing layer of an La_2O_3/SnO_2 stack and platinum interdigitated electrodes. The electrodes have a width of 10 μm and a spacing of 20 μm.

First, SiO_2 with a thickness of approximately 620 nm was thermally grown on a Si substrate. A 100-nm-thick SiN was then deposited by low-pressure chemical vapor deposition (LPCVD). Poly-Si with a thickness of approximately 330 nm was deposited on the SiN/SiO_2 layer by LPCVD. The phosphorus doping was carried out by thermal diffusion using phosphorus oxychloride gas at 1050 °C. The sheet resistance of the doped poly-Si was approximately 17 Ω/sq, which corresponded

to the resistivity of 5.6×10^{-4} Ω cm. Poly-Si was then patterned by reactive ion etching to form the heater resistor. A SiN layer with a thickness of 100 nm was deposited by LPCVD, as an insulation layer between the heater and the sensor. A Pt/Ti layer was then deposited by sputtering and patterned by a lift-off process to form the electrode. The Pt/Ti layer was also used as a wiring of the heater. As a protective layer of the wiring, an SiO_2 layer was deposited by plasma-enhanced CVD. The thickness of the SiO_2 layer was approximately 500 nm. After exposing the sensing electrodes by etching the SiO_2 layer to define the sensing area, SnO_2 was deposited by sputtering, and its thickness was approximately 100 nm. For La_2O_3 deposition, metal-organic decomposition material (La-03, Kojundo Chemical Lab. Co., Sakado, Japan) was used as a precursor and was spin-coated on the sample with a rotational speed of 4000 rpm. Then, the sample was prebaked at 200 °C in the air for 30 min, followed by rapid thermal annealing (RTA) at 650 °C in an O_2 atmosphere for 70 s. The area of the sensing material was 110 µm $\times$ 110 µm, which was patterned by a liftoff process. Finally, the membrane was released by deep-reactive ion etching followed by xenon difluoride etching from the backside. The membrane area was 140 µm $\times$ 140 µm, and the effective area of the device including the bridges was approximately 270 µm $\times$ 270 µm. The fabrication details of the MHP are described elsewhere [28].
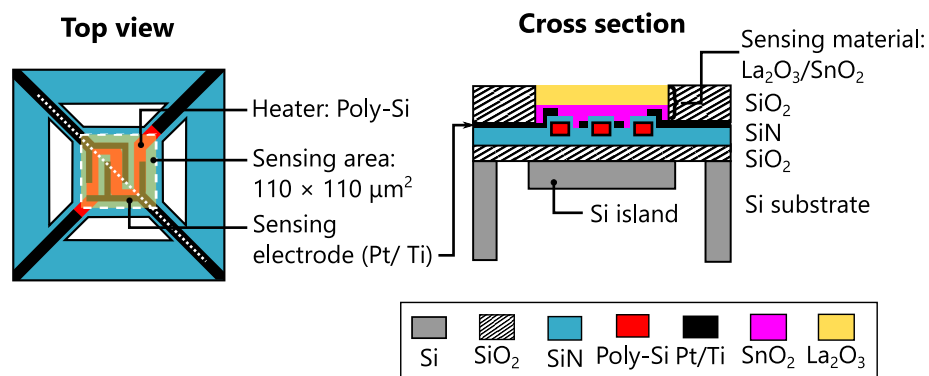

Figure 1. Schematic illustration of the device. The left and right figures represent its top and cross-sectional views, respectively. The location of the cross section is indicated as a white dotted line in the top view. Note that the upper SiO_2 layer is not shown in the top view for the ease of understanding.

2.2. Measurement Procedure

The structure of the sensing layer was observed by scanning electron microscopy (SEM) with an acceleration voltage of 10 kV. The observation was conducted on the sensor elements fabricated on SiO_2/Si substrates (not on the MHP).

Electrical measurements were performed in a chamber with a gas-control system, as shown in Figure 2. The chamber has two gas inlets and one outlet, and the atmosphere in the chamber was controlled by changing the flow rate of the used gases. The system has three gas lines (N_2, O_2, and CO_2), and these gas flows were controlled by flow meters for N_2 and O_2, and a mass-flow controller for CO_2. In the chamber, the current flowing through the sensing elements was measured by applying a bias voltage of 0.5 V. During the measurements, a mixture of N_2 and O_2, as synthesized air, was introduced into the chamber with a constant flow rate (N_2: 1.6 slm and O_2: 0.4 slm). Then, CO_2 was introduced into the chamber to investigate the CO_2 response at various CO_2 concentrations and heater temperatures, at which the CO_2 concentration was set by controlling the flow rate of CO_2. The CO_2 response was defined as the quotient of the resistance in the atmosphere without CO_2 (R_a) and with CO_2 (R_{CO_2}), R_a/R_{CO_2}.
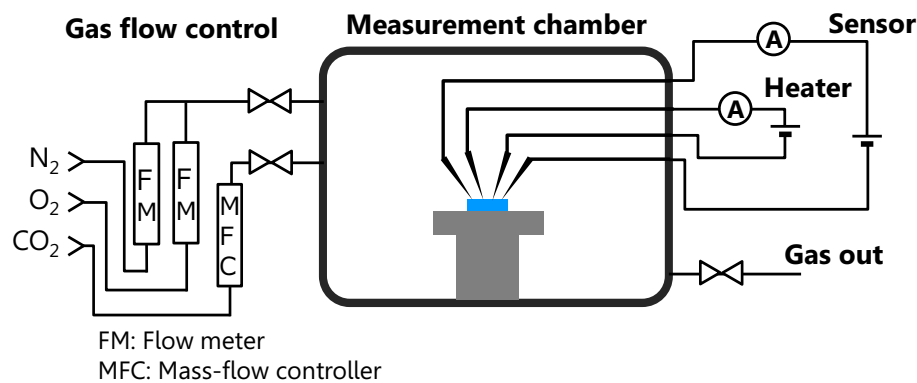
Figure 2. Schematic illustration of the measurement system. Three gas lines (N_2, O_2, and CO_2) are equipped with the system, and these gases are introduced into the chamber through flow meters and a mass–flow controller.

3. Results and Discussion

3.1. Observation of the Sensing Layer

Figure 3a shows an SEM image of the SnO_2 layer. The SnO_2 layer has a compact structure with a grain size range of 20–40 nm. Figure 3b,c depict the images of the La_2O_3/SnO_2 layer at different magnifications. The images (b) and (c) reveal that the La_2O_3 layer was discontinuously deposited on the SnO_2 layer, which was partly exposed to the atmosphere. In addition, the grain structure was not clear in the La_2O_3 layer. The discontinuous layer of La_2O_3 may have resulted from the deposition condition including a spin-coating, a lift-off process, and RTA. Given that CO_2 responses change with the concentration of La_2O_3 in the mixture of La_2O_3 and SnO_2 [10], the coverage of the La_2O_3 layer possibly influences the response to CO_2 and the selectivity, and thus, the deposition condition of La_2O_3 layer should be investigated. Nevertheless, the situation that both the SnO_2 and La_2O_3 layer were exposed to the atmosphere is similar to previous studies [10,14]. Thus, sensitization by the La_2O_3 layer should be obtained in this regard.
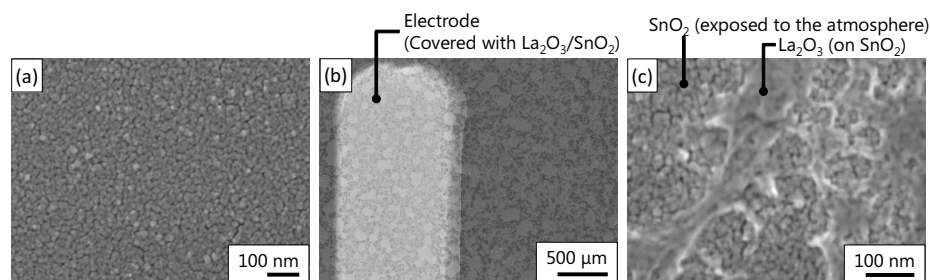

Figure 3. Scanning electron microscopy images of the material: (**a**) SnO_2 surface; (**b**) La_2O_3/SnO_2 surface; and (**c**) the magnified image of (**b**).

3.2. Characteristics of Micromachined Hotplates

As the optical microscope image in Figure 4 shows, the device was successfully fabricated. Then, the heater of the MHP was characterized. Figure 5a shows the current–voltage ($I - V$) characteristics of the heater. In addition, the heater temperature calculated from the heater resistance [28] was plotted on the graph. It was confirmed that the MHP can be heated to approximately 530 °C at 5 V. The heater temperature plotted against the power consumption of the heater is shown in Figure 5b. The characteristics show that the power consumption at 400 °C, which is a typical operating temperature of semiconductor CO_2 sensors, was approximately 23 mW.
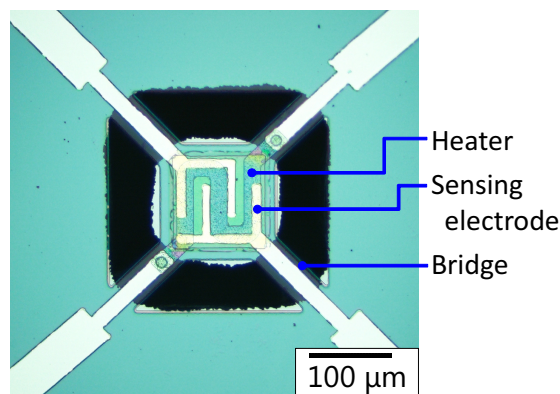
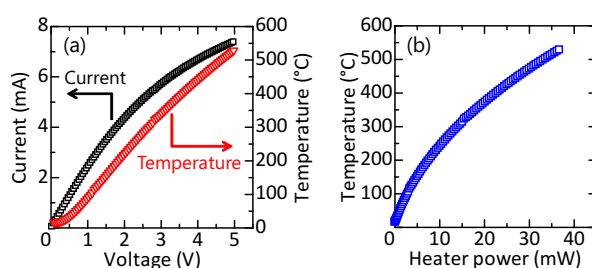**Figure 4.** Optical microscopy image of the fabricated device.

Figure 5. (**a**) $I - V$ characteristics of the heater. The corresponding temperature calculated from the heater resistance is also plotted; (**b**) The temperature of the heater plotted against the power consumption.

3.3. Temperature Dependence of the CO_2-Sensing Characteristics

The response for 1000-ppm CO_2 obtained from the resistance–time ($R - t$) characteristics at different temperatures is shown in Figure 6. The result for the SnO_2 element is also shown for comparison. In both elements, the response increased as the temperature increased, reached a peak value at a certain temperature, and then decreased with further increasing temperature. The response of the La_2O_3/SnO_2 element was smaller than that of SnO_2 at low temperatures (e.g., near 250 °C), while it exceeds that of the SnO_2 element above 250 °C. The maximum response of approximately 2.9 was obtained near 350 °C for the La_2O_3/SnO_2 element, whereas the SnO_2 element exhibited a maximum response of 2.2 near 400 °C. Above 450 °C, the response of both elements decreased with increasing temperature, and they exhibited similar responses. As a result, a higher maximum response was obtained for the La_2O_3/SnO_2 element, namely, sensitization by La_2O_3 was obtained in the device on the MHP. The power consumption at 350 °C of the MHP was approximately 17 mW, which is smaller by approximately one order of magnitude than that of the conventional semiconductor sensors [29].

For the SnO_2 element, it is reasonable to ascribe the CO_2 response to the chemical adsorption (chemisorption) of CO_2 on the surface. In contrast, given that the sensitization by the deposition of La_2O_3 was observed, the chemisorption of CO_2 on the La_2O_3 plays an important role in the response of the La_2O_3/SnO_2 element. It was suggested that carbonate formation by the reaction between La_2O_3 and CO_2 is the main cause of the CO_2 response [11,30], and the suggested reactions are as follows [30].

$$O^{2-} + CO_2 \rightarrow CO_3^{2-} \tag{1}$$

$$CO_2 + CO_3^{2-} \rightarrow C_2O_4 + O^{2-} \tag{2}$$

On the other hand, because the La_2O_3 layer is discontinuous and La_2O_3 generally exhibits much larger resistivity than SnO_2, almost all the current should flow through the SnO_2 layer, while La_2O_3 acts as a sensitization layer in this study. Thus, carrier density in the SnO_2 layer must be modulated accompanying to the above reactions, whereas these reactions do not directly cause carrier transfer. Although the detailed mechanism of the carrier transfer is not clear and should be further investigated, one possible scenario is the trap/detrap of carriers from the states at the interface between SnO_2 and La_2O_3. It is likely that the work function of La_2O_3 is changed by the CO_2 chemisorption at the surface, and this work function change might be related to the trap/detrap of carriers.
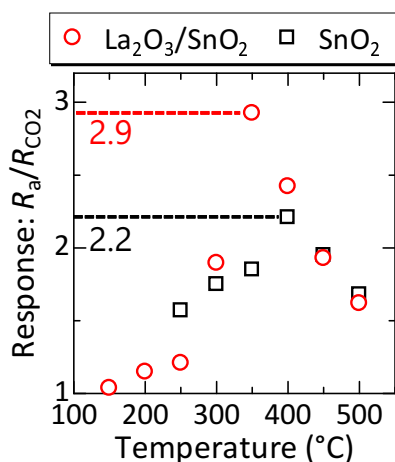

Figure 6. Temperature dependence of the CO_2 response of the sensors. The sensitivities of both SnO_2 and La_2O_3/SnO_2 elements are plotted. SnO_2 showed the highest response of 2.2 near 400 °C, whereas La_2O_3/SnO_2 showed a higher response of 2.9 than SnO_2 near 350 °C.

Here, the temperature dependence of the response is discussed. These chemisorption is generally a thermally activated process, competing with physical adsorption (physisorption), and, therefore, as temperature increased, the probability of chemisoption increases [31]. On the contrary, by further increasing the temperature, desorption of the molecule may become dominant, resulting in the response being decreased at higher temperature. The activation energy for chemisorption and desorption of CO_2 depends on the adsorbate, causing a difference in the temperature dependence of the response between SnO_2 and La_2O_3/SnO_2. CO_2 chemisorption on SnO_2 can occur at low temperatures [32], and the two kinds of activation energy for the desorption were reported as 0.18 and 0.06 eV. The energy for chemisorption should be smaller than those energies. On the other hand, Esaka et al. conducted differential thermal analysis (DTA), and reported that the significant adsorption of CO_2 on Bi_2O_3–La_2O_3 under CO_2 atmosphere occurred near 400 °C [33]. Bakiz et al. reported that the transformation of La_2O_3 to $La_2O_2CO_3$ (carbonatation) occurred near 520 °C [34], and the activation energy for the carbonatation at the oxide surface to be 7.6 eV. Although these specific temperatures, which depend on the material and experimental conditions, are just for reference, it is likely that the CO_2 chemisorption on La_2O_3 has larger activation energy than that on SnO_2. Therefore, the probability of CO_2 chemisorption on La_2O_3 may be small at low temperatures, and the response to CO_2 at low temperatures may be larger in the SnO_2 than in La_2O_3/SnO_2.

Concerning the response decrease at high temperatures, Marsal et al. reported that the CO_2 desorption from LaOCl was observed in the temperature range of 260–380 °C by TPD analysis [30]. Given that the desorption temperature depends on the material and microscopic surface structure, as just mentioned, the temperature at which the CO_2 response began to decrease in this study (above 350 °C) roughly corresponds to such a desorption temperature. As a result, the response may reach the maximum near 350 °C in this study. Similar temperature dependencies, in which the response reached a maximum at a certain temperatures, were also reported in previous studies on La-compound-based

CO_2 sensors [14,35]. In contrast, for SnO_2, Dobrovolsky et al. reported that the thermal desorption spectrum of CO_2 adsorbed on SnO_2 at 20 °C exhibited a desorption peak near 400 °C. Although the temperature for the maximum response of the SnO_2 element is speculated to be lower than that of La_2O_3/SnO_2 because of the smaller activation energy for CO_2 desorption from SnO_2 than that from La_2O_3 (activation energy for desorption is generally larger than that for chemisorption), taking account of the study in Ref. [32], it might be possible that the SnO_2 element exhibited a maximum response to approximately 400 °C.

Table 2 compares the properties of the La-compound-based CO_2 sensor with those in the previous studies. As shown in Table 2, the response of the sensor in this work is high, although it is not the highest. Further, our device operates with low power consumption owing to the MHP, whereas the others are not fabricated on MHPs. Namely, this work demonstrates a semiconductor CO_2 sensor with both a fairly good response and low power consumption. Note that the MHP is heated to a driving temperature (several hundreds °C) with a short period (~100 ms) due to its small thermal capacity. Thus, intermittently driving the sensor with short pulse inputs is possible, which enables a further decrease in the power consumption, as demonstrated in Ref. [36]. Furthermore, the MHP-based sensors are also beneficial to improve selectivity, which is one the most critical properties of gas sensors. The sensor in this study is likely to have poor selectivity to other reducing gases such as CO and H_2 because the SnO_2 layer was partly exposed to the air. For this issue, using a reference sensor and reading differential output between the sensor and the reference is one solution. However, using a reference sensor is rather problematic for conventional metal oxide sensors because it causes an increase in module size and the power consumption. In contrast, MHP-based sensors allow us to easily integrate multiple elements into a single chip, because they are fabricated by a monolithic IC process. Therefore, in conjunction with their capability of low-power operation, it is possible to improve the selectivity as a chip by realizing such an array in which a sensor and a reference are simultaneously integrated, while also keeping their advantages of miniature size and low power consumption.

Table 2. Comparison of the properties of La-compound-based CO_2 sensors.

Material	Response for 1000-ppm CO_2	Temperature	MHP	Ref.
La_2O_3-SnO_2	1.5 [a]	400 °C	−	[9]
La_2O_3-SnO_2	1.2	400 °C	−	[10]
LaOCl	2.9	260 °C	−	[35]
LaOCl-SnO_2 NW	4.5	400 °C	−	[14]
La_2O_3/SnO_2	2.9	350 °C	+	This work

[a]: for approximately 1100-ppm CO_2.

Another interesting result is that the relatively high response was obtained for a sputtered-SnO_2 film, which formed a compact layer, as shown in Figure 3. Generally, porous layers show higher response than compact layers due to their large surface–volume ratio for reducing gases such as CO and H_2 [25,27]. Despite that, our device showed a relatively high response (see Table 2). We ascribe this response to the contribution of the resistance near the electrode contacts. In compact layers, the resistance component near the contact tends to become large as compared with that in porous films because the resistance at the grain boundaries can be small in compact layers. Thus far, several studies reported the contribution of the resistance near the contacts to the detection [37,38]. Hoefer et al. have shown that the resistance near the contacts significantly contributed to detection in sputtered films [37]. In a similar manner, the contribution of the resistance near the contacts may be significant in this study, thus, a higher response was obtained than in other studies in which porous thick films were used. In addition, it is indicative that the LaOCl-functionalized SnO_2-NW showed a high response, in which the SnO_2-NW was more than 10 μm long, and the electrode gap was 20 μm [14]. Because the length of the NW and the electrode gap were of the same order of magnitude, the number of the contacts between NWs become much less than the number of grain boundaries in porous layers. As a result,

the component of the contact resistance can become large, which may contribute to the high response. Further investigation of the effect of the resistance near the contacts on CO_2 detection is under way.

3.4. Concentration Dependence of the CO_2 Response

The response of the sensor for different CO_2 concentrations was measured at 400 °C, at which the power consumption of the heater was approximately 23 mW. Figure 7 shows the time-dependent resistance change of the La_2O_3/SnO_2 element when it was exposed to CO_2 with different concentrations: (a) 200–1000 ppm and (b) 1500–4000 ppm. Note that the measurement was interrupted between (a) and (b) because of the limitation of the measuring instrument. Although a baseline resistance drift was observed, the magnitude of resistance change increased with the increasing CO_2 concentration. The response was calculated from the ratio between the average resistance during CO_2 exposure and baseline resistance for which the drift component was taken into account.
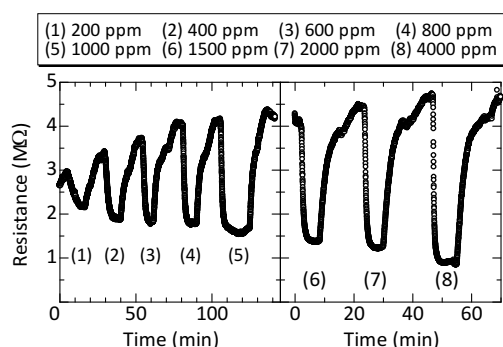

Figure 7. Time-dependent resistance change of the La_2O_3/SnO_2 element for different CO_2 concentrations. The measurement was interrupted between (5) and (6) for several tens of a second because of the limitation of the measuring instrument.

The obtained response was plotted against CO_2 concentration, as shown in Figure 8. In the measured concentration range, the response increased with CO_2 concentration without saturation. Furthermore, it was demonstrated that a minimum amount of 200 ppm of CO_2 was distinguishable in this study. Note that 200 ppm was the least measurement step in this study, and thus the device in this study has the potential of a better resolution, less than 200 ppm. Consequently, these results, including the discussion in Section 3.3, indicate the promising properties of the device in this study for smart CO_2 sensors.
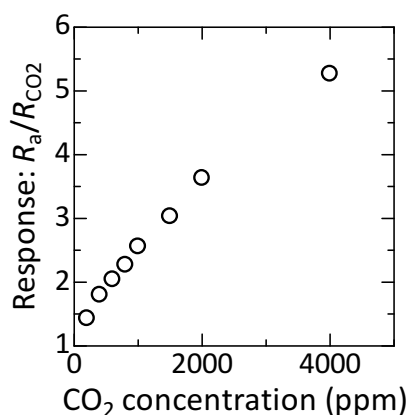

Figure 8. CO_2 concentration dependence of the response at 400 °C.

4. Conclusions

In this study, MHP-based CO_2 sensors for smart sensors were characterized. The sensor comprised a La_2O_3/SnO_2 stacked layer with Pt interdigitated electrodes, fabricated on a bridge-type MHP. SnO_2 grains with a size of 20–40 nm formed a compact layer, whereas the La_2O_3 layer was discontinuously deposited on the SnO_2 layer. The fabricated sensor showed a response of 2.9 for 1000-ppm CO_2, which was relatively high compared with previously reported values. The resistance near the electrode contacts was suggested to significantly contribute to the response, causing a high response. Furthermore, CO_2 detection was successfully performed in the range of 200–4000 ppm, and it was revealed that a minimum amount of 200-ppm CO_2 was distinguishable by the sensor. The device in this study demonstrated promising properties for miniature low-power CO_2 sensors toward smart sensing.

References

1. Hagleitner, C.; Hierlemann, A.; Lange, D.; Kummer, A.; Kerness, N.; Brand, O.; Baltes, H. Smart single-chip gas sensor microsystem. *Nature* **2001**, *414*, 293–296.
2. Barrettino, D.; Graf, M.; Zimmermann, M.; Hagleitner, C.; Hierlemann, A.; Baltes, H. A Smart Single-Chip Micro-Hotplate-Based Gas Sensor System in CMOS-Technology. *Analog Integr. Circuits Signal Process.* **2004**, *39*, 275–287.
3. Maeng, S.; Guha, P.; Udrea, F.; Ali, S.Z.; Santra, S.; Gardner, J.; Park, J.; Kim, S.H.; Moon, S.E.; Park, K.H.; et al. SOI CMOS-Based Smart Gas Sensor System for Ubiquitous Sensor Networks. *ETRI J.* **2008**, *30*, 516–525.
4. Product Specification CO_2 Engin® K30 STA. Available online: http://www.senseair.com/wp-content/uploads/2015/03/CO2-Engine-K30_PSP110-R7.pdf (accessed on 28 August 2017).
5. Lee, H.J.; Park, K.K.; Kupnik, M.; Khuri-Yakub, B.T. Functionalization layers for CO_2 sensing using capacitive micromachined ultrasonic transducers. *Sens. Actuators B Chem.* **2012**, *174*, 87–93.
6. Currie, J.; Essalik, A.; Marusic, J.C. Micromachined thin film solid state electrochemical CO_2, NO_2 and SO_2 gas sensors. *Sens. Actuators B Chem.* **1999**, *59*, 235–241.
7. Sahner, K.; Schulz, A.; Kita, J.; Merkle, R.; Maier, J.; Moos, R. CO_2 Selective Potentiometric Sensor in Thick-film Technology. *Sensors* **2008**, *8*, 4774–4785.
8. Morio, M.; Hyodo, T.; Shimizu, Y.; Egashira, M. Effect of macrostructural control of an auxiliary layer on the CO_2 sensing properties of NASICON-based gas sensors. *Sens. Actuators B Chem.* **2009**, *139*, 563–569.
9. Mizuno, N.; Yoshioka, T.; Kato, K.; Iwamoto, M. CO_2-sensing characteristics of SnO_2 element modified by La_2O_3. *Sens. Actuators B Chem.* **1993**, *13*, 473–475.
10. Kim, D.H.; Yoon, J.Y.; Park, H.C.; Kim, K.H. CO_2-sensing characteristics of SnO_2 thick film by coating lanthanum oxide. *Sens. Actuators B Chem.* **2000**, *62*, 61–66.
11. Marsal, A.; Cornet, A.; Morante, J. Study of the CO and humidity interference in La doped tin oxide CO_2 gas sensor. *Sens. Actuators B Chem.* **2003**, *94*, 324–329.
12. Liao, B.; Wei, Q.; Wang, K.; Liu, Y. Study on $CuO–BaTiO_3$ semiconductor CO_2 sensor. *Sens. Actuators B Chem.* **2001**, *80*, 208–214.
13. Herrán, J.; Mandayo, G.G.; Castaño, E. Physical behaviour of $BaTiO_3–CuO$ thin-film under carbon dioxide atmospheres. *Sens. Actuators B Chem.* **2007**, *127*, 370–375.
14. Trung, D.D.; Toan, L.D.; Hong, H.S.; Lam, T.D.; Trung, T.; Van Hieu, N. Selective detection of carbon dioxide using LaOCl-functionalized SnO_2 nanowires for air-quality monitoring. *Talanta* **2012**, *88*, 152–159.
15. Hafiz, S.M.; Ritikos, R.; Whitcher, T.J.; Razib, N.M.; Bien, D.C.S.; Chanlek, N.; Nakajima, H.; Saisopa, T.; Songsiriritthigul, P.; Huang, N.M.; et al. A practical carbon dioxide gas sensor using room-temperature hydrogen plasma reduced graphene oxide. *Sens. Actuators B Chem.* **2014**, *193*, 692–700.

16. Lin, Z.D.; Young, S.J.; Chang, S.J. CO_2 Gas Sensors Based on Carbon Nanotube Thin Films Using a Simple Transfer Method on Flexible Substrate. *IEEE Sens. J.* **2015**, *15*, 7017–7020.

17. Srinives, S.; Sarkar, T.; Hernandez, R.; Mulchandani, A. A miniature chemiresistor sensor for carbon dioxide. *Anal. Chim. Acta* **2015**, *874*, 54–58.

18. Simon, I.; Bârsan, N.; Bauer, M.; Weimar, U. Micromachined metal oxide gas sensors: Opportunities to improve sensor performance. *Sens. Actuators B Chem.* **2001**, *73*, 1–26.

19. Barrettino, D.; Graf, M.; Taschini, S.; Hafizovic, S.; Hagleitner, C.; Hierlemann, A. CMOS Monolithic Metal-Oxide Gas Sensor Microsystems. *IEEE Sens. J.* **2006**, *6*, 276–286.

20. Gardner, J.W.; Guha, P.K.; Udrea, F.; Covington, J.A. CMOS Interfacing for Integrated Gas Sensors: A Review. *IEEE Sens. J.* **2010**, *10*, 1833–1848.

21. Sheng, L.Y.; Tang, Z.; Wu, J.; Chan, P.C.H.; Sin, J.K.O. A low-power CMOS compatible integrated gas sensor using maskless tin oxide sputtering. *Sens. Actuators B Chem.* **1998**, *49*, 81–87.

22. Briand, D.; Krauss, A.; van der Schoot, B.; Weimar, U.; Barsan, N.; Göpel, W.; de Rooij, N.F. Design and fabrication of high-temperature micro-hotplates for drop-coated gas sensors. *Sens. Actuators B Chem.* **2000**, *68*, 223–233.

23. Chan, P.C.H.; Yan, G.Z.; Sheng, L.Y.; Sharma, R.K.; Tang, Z.; Sin, J.K.O.; Hsing, I.M.; Wang, Y. An integrated gas sensor technology using surface micro-machining. *Sens. Actuators B Chem.* **2002**, *82*, 277–283.

24. Ivanov, P.; Laconte, J.; Raskin, J.P.; Stankova, M.; Sotter, E.; Llobet, E.; Vilanova, X.; Flandre, D.; Correig, X. SOI-CMOS compatible low-power gas sensor using sputtered and drop-coated metal-oxide active layers. *Microsyst. Technol.* **2005**, *12*, 160–168.

25. Yamazoe, N. New approaches for improving semiconductor gas sensors. *Sens. Actuators B* **1991**, *5*, 7–19.

26. Barsan, N.; Schweizer-Berberich, M.; Göpel, W. Fundamental and practical aspects in the design of nanoscaled SnO_2 gas sensors: A status report. *Fresenius J. Anal. Chem.* **1999**, *365*, 287–304.

27. Korotcenkov, G. The role of morphology and crystallographic structure of metal oxides in response of conductometric-type gas sensors. *Mater. Sci. Eng. R* **2008**, *61*, 1–39.

28. Iwata, T.; Soo, W.P.C.; Matsuda, K.; Takahashi, K.; Ishida, M.; Sawada, K. Design, fabrication, and characterization of bridge-type micro-hotplates with an SU-8 supporting layer for a smart gas sensing system. *J. Micromech. Microeng.* **2017**, *27*, 024003.

29. Figaro Engineering Inc. Available online: http://www.figaro.co.jp/en/ (accessed on 28 August 2017).

30. Marsal, A.; Centeno, M.; Odriozola, J.; Cornet, A.; Morante, J. DRIFTS analysis of the CO_2 detection mechanisms using LaOCl sensing material. *Sens. Actuators B* **2005**, *108*, 484–489.

31. Wolkenstein, T. *Electronic Processes on Semiconductor Surfaces during Chemisorption*; Springer: Boston, MA, USA, 1991.

32. Dobrovolsky, Y.; Zyubina, T.; Kalinnikov, G. Chemisorption of CO_2 at oxide electrodes in the presence of oxygen and water. *Ionics* **1995**, *1*, 358–365.

33. Esaka, T.; Moto-ike, K. CO_2 absorption and desorption of Bi_2O_3–La_2O_3 powders prepared by mechanical synthesis. *Mater. Res. Bull.* **2004**, *39*, 1581–1587.

34. Bakiz, B.; Guinneton, F.; Arab, M.; Benlhachemi, A.; Villain, S.; Satre, P.; Gavarri, J.R. Carbonatation and Decarbonatation Kinetics in the La_2O_3–$La_2O_2CO_3$ System under CO_2 Gas Flows. *Adv. Mater. Sci. Eng.* **2010**, *2010*, 360597.

35. Marsal, A.; Dezanneau, G.; Cornet, A.; Morante, J. A new CO_2 gas sensing material. *Sens. Actuators B* **2003**, *95*, 266–270.

36. Tabata, S.; Higaki, K.; Ohnishi, H.; Suzuki, T.; Kunihara, K.; Kobayashi, M. A micromachined gas sensor based on a catalytic thick film/SnO_2 thin film bilayer and a thin film heater Part 2: CO sensing. *Sens. Actuators B Chem.* **2005**, *109*, 190–193.

37. Hoefer, U.; Steiner, K.; Wagner, E. Contact and sheet resistance of SnO_2 thin films from transmission-line model measurements. *Sens. Actuators B Chem.* **1995**, *26*, 59–63.

38. Tamaki, J.; Miyaji, A.; Makinodan, J.; Ogura, S.; Konishi, S. Effect of micro-gap electrode on detection of dilute NO_2 using WO_3 thin film microsensors. *Sens. Actuators B Chem.* **2005**, *108*, 202–206.